POLITECNICO DI MILANO

SCHOOL OF INDUSTRIAL AND INFORMATION ENGINEERING

MSc of Mathematical Engineering

Project for the course *Numerical analysis for partial differential equations*

Numerical study of Euler equations in supersonic flow over a double-wedge airfoil

Giuseppe ORLANDO

Matr. 878776

Contents

Introduction

In this work we consider the computation of a supersonic flow over a double-wedge airfoil.
The presence of this kind of bodies in supersonic flow field creates singularities in our flow such as shocks and expansion waves; in this condition the main aerodynamics coefficients, in particular the drag, increase and we must be able to predict their value in order to keep under control the behaviour of our system in various flight conditions.
The main aim of this project is to show how a discontinuous Galerkin method is able to guarantee for a such complex flow field results in the aerodynamic response which are in good agreement with theoretical and experimental data.

We begin by reviewing the governing equations in Section 1, then we present the weak formulation and the finite element formulation in Section 2 and 3 respectively, while the numerical method employed for the simulation will be proposed in Section 4.
Finally we apply what we found in the previous sections to the simulation of a supersonic flow over a double-wedge airfoil to display the performance of the method.

1. The governing equations

In the current study we are simulating a very high speed flow over an airfoil and this means that viscous effects can be neglected; for this reason, in order to simplify in a remarkable way the problem, unsteady Euler equations that govern a compressible inviscid flow are solved: they consist of conservation laws of mass (1.1), momentum (1.2) and energy (1.3).

Let $\Omega \subset \mathbb{R}^2$ be the bounded spatial domain, $(0, T)$ be the temporal range and let $\partial\Omega$ denote the boundary of Ω which is assumed to be piecewise smooth Lipschitz. The spatial and temporal coordinates are denoted by $\boldsymbol{x} = (x_1, x_2)^T$ and t respectively.
First of all we point out that in this project we will start from the Euler equations in *conservative* form which means that every conservation law can be expressed in the form:

$$\frac{\partial Q}{\partial t} + \nabla \cdot \boldsymbol{F}(Q) = S$$

where $\nabla\cdot$ denotes the divergence operator.
Here Q is the conserved variable, $\boldsymbol{F}$ is the flux and S is the source term; with this kind of formulation the integral form allows discontinuous solutions (while non-conservative form allows only smooth differentiable solutions) and since in this phenomenon we expect a shock wave it is fundamental to be able to catch this behaviour and we will see which finite element formulation is more suitable for this purpose.

The Euler equations governing the fluid flow, in conservative form, are:

$$\frac{\partial \rho}{\partial t} + \nabla \cdot (\rho \boldsymbol{u}) = 0 \quad \text{in } \Omega, t > 0 \tag{1.1}$$

$$\frac{\partial (\rho \boldsymbol{u})}{\partial t} + \nabla \cdot (\rho \boldsymbol{u} \otimes \boldsymbol{u} + p \overleftrightarrow{\boldsymbol{I}}) = \rho \boldsymbol{f} \quad \text{in } \Omega, t > 0 \tag{1.2}$$

$$\frac{\partial (\rho E)}{\partial t} + \nabla \cdot ((\rho E + p)\boldsymbol{u}) = \rho(\boldsymbol{f} \cdot \boldsymbol{u} + r) \text{ in } \Omega, t > 0 \tag{1.3}$$

completed with suitable initial and boundary conditions.

Here, $\rho, \boldsymbol{u}, p, E, \boldsymbol{f}$ and r are the density, the velocity, the pressure, the total energy per unit of mass, the external force per unit of mass and the internal energy production per unit of mass respectively, while $\overleftrightarrow{\boldsymbol{I}}$ denotes the identity tensor.

The total energy is the sum of two contributions: the kinetic energy per unit of mass and the internal energy per unit of mass e, namely:

$$E = \frac{1}{2} |\boldsymbol{u}|^2 + e$$

In order to close the model we need eventually to give a relation between thermodynamic variables: the equation of state.
In this example we treat dry air as a thermally perfect gas whose equation of state assumes the special form:

$$p = (\gamma - 1)\rho e$$

where γ is the ratio between the specific heat at constant pressure and the specific heat at constant volume and it is equal to 1.4.
As final assumption we consider our fluid not subjected to external forces, which means $\boldsymbol{f} = \mathbf{0}$ and $r = 0$.

2. Weak formulation

The compressible Euler equations presented in the previous section can be written in system form as:

$$\frac{\partial \boldsymbol{U}}{\partial t} + \sum_{i=1}^{2} \frac{\partial \boldsymbol{F_i}}{\partial x_i} = 0 \quad \text{in } \Omega, t > 0 \quad i = 1, 2$$

$\boldsymbol{U}$ is the vector of conserved variables defined as:

$$\boldsymbol{U} = (\rho, \rho u_1, \rho u_2, \rho E)^T$$

while $\boldsymbol{F_i}$ denote the convective (Euler) flux whose components are defined as:

$$\boldsymbol{F_1} = \left(\rho u_1, \rho u_1^2 + p, \rho u_1 u_2, (\rho E + p)\, u_1\right)^T$$
$$\boldsymbol{F_2} = \left(\rho u_1, \rho u_1 u_2, \rho u_2^2 + p, (\rho E + p)\, u_2\right)^T$$

Here u_1 and u_2 are the components of velocity along x_1 and x_2 direction respectively.
Moreover we equipe this system with initial and boundary conditions. We prescribe the initial condition

$$\boldsymbol{U}(\boldsymbol{x}, 0) = \boldsymbol{U_0}(\boldsymbol{x}) \qquad \text{in } \Omega$$

where $\boldsymbol{U_0}$ is a given vector-value function.
The boundary conditions are given formally by

$$\boldsymbol{BU} = \boldsymbol{G} \qquad \text{on } \partial\Omega \times (0, T)$$

Here $\boldsymbol{B}$ denotes a generally boundary operator and $\boldsymbol{G}$ is a vector-value function for boundary conditions.
The choice of appropriate boundary conditions is a very delicate issue in the simulation of the numerical flow and this holds in particular for the case of Euler equations.
In our context we distinguish three disjoint parts of the boundary $\partial\Omega$, namely $\partial\Omega_i$ for the inlet, $\partial\Omega_o$ for the outlet and $\partial\Omega_w$ for the impermeable walls. We will discuss later on the meaning and the numerical treatment for these kind of boundaries.

Let $H^1(\Omega)$ be the space of functions that are square integrable together with their first-order derivatives in our domain Ω.
Let us denote by $\boldsymbol{V}$ the following vector space:

$$\boldsymbol{V} = H^1(\Omega) \times [H^1(\Omega)]^2 \times H^1(\Omega)$$

The weak formulation can be written as follows:

$\forall t > 0$, find $\boldsymbol{U}(t) \in \boldsymbol{V}$ such that $\forall \boldsymbol{v} \in \boldsymbol{V}$

$$\int_\Omega \left(\frac{\partial \boldsymbol{U}}{\partial t} + \sum_{i=1}^{2} \frac{\partial \boldsymbol{F_i}}{\partial x_i} \right) \cdot \boldsymbol{v} \, d\Omega = 0 \qquad i = 1, 2 \tag{2.1}$$

with $\boldsymbol{U}(0) = \boldsymbol{U_0}(\boldsymbol{x})$.

We integrate by parts the convective flux and we get:

$$\int_\Omega \frac{\partial \boldsymbol{F_i}}{\partial x_i} \cdot \boldsymbol{v} \, d\Omega = - \int_\Omega \frac{\partial \boldsymbol{v}}{\partial x_i} \cdot \boldsymbol{F_i} \, d\Omega + \int_{\partial\Omega} \boldsymbol{v} \cdot \boldsymbol{F_i} n_i \, d\Gamma \qquad i = 1, 2$$

where n_i is the i-th component of the outward unitary normal.
If we substitute in equation (2.1) the previous results we get the following weak formulation:

$\forall t > 0$, find $\boldsymbol{U}(t) \in \boldsymbol{V}$, such that $\forall \boldsymbol{v} \in \boldsymbol{V}$

$$\int_\Omega \frac{\partial \boldsymbol{U}}{\partial t} \cdot \boldsymbol{v} \, d\Omega = \int_\Omega \sum_{i=1}^{2} \boldsymbol{F_i} \cdot \frac{\partial \boldsymbol{v}}{\partial x_i} \, d\Omega - \int_{\partial\Omega} \sum_{i=1}^{2} \boldsymbol{F_i} ni \cdot \boldsymbol{v} \, d\Omega \tag{2.2}$$

with $\boldsymbol{U}(0) = \boldsymbol{U_0}(\boldsymbol{x})$.

For the sake of clarity the governing equation in the weak form for each conserved variable is written; the mass balance equation is:

$$\int_\Omega \frac{\partial \rho}{\partial t} \tilde{w} \, d\Omega = \int_\Omega \sum_{i=1}^{2} (\rho u_i) \frac{\partial \tilde{w}}{\partial x_i} - \int_{\Gamma_N} \sum_{i=1}^{2} (\rho u_i) n_i \tilde{w} \, d\Omega = 0, \qquad \forall \tilde{w} \in H^1(\Omega)$$

The momentum conservation is

$$\int_\Omega \frac{\partial (\rho u_j)}{\partial t} \tilde{v} \, d\Omega = \int_\Omega \sum_{i=1}^{2} \rho u_i u_j \frac{\partial \tilde{v}}{\partial x_i} \, d\Omega - \int_{\Gamma_N} \sum_{i=1}^{2} (\rho u_i u_j n_i) \, \tilde{v} \, d\Gamma = 0, \qquad \forall \tilde{v} \in H^1(\Omega), \quad j = 1, 2$$

and the energy conservation is

$$\int_\Omega \frac{\partial (\rho E)}{\partial t} \tilde{z} \, d\Omega = \int_\Omega \sum_{i=1}^{2} \left(u_i (\rho E + p) \frac{\partial \tilde{z}}{\partial x_i} \right) \, d\Omega - \int_{\Gamma_N} \sum_{i=1}^{2} ((\rho E + p) u_i n_i) \, \tilde{z} \, d\Gamma = 0, \qquad \forall \tilde{z} \in H^1(\Omega).$$

3. Discontinuous Galerkin semidiscretization

As discussed in Section 1 the solution of Euler equations often shows discontinuities and the ability to handle the discontinuities automatically as part of the solution procedure is a desired property; for this reason finite volume methods are traditionally used because of its natural conservative properties.
However these methods are difficult to make higher order in space while it would be really important to develop high-order schemes to solve this kind of equations that appear in many practical applications where convection plays a key role such as meteorology, weather forecasting or gas dynamics.
The appeal of discontinuous Galerkin method is that it is possible to achieve high-order accuracy as it is typical of finite element framework with the capability to allow discontinuities across cell interfaces and thus discontinuous solutions.

Consider now a discretization of Ω into a family of triangulations $\mathcal{T}_h$ and we denote by K each element.
Moreover we denote by h_K the diameter of each element K where

$$\text{diam}(K) = \max_{\boldsymbol{x},\boldsymbol{y}\in K} |\boldsymbol{x}-\boldsymbol{y}| \qquad \forall K \in \mathcal{T}_h$$

and we define $h = \max_{K\in\mathcal{T}_h} h_K$.
Further the symbol $\mathcal{T}_h^I$ stands for the set of all edges $\Gamma \in \mathcal{T}_h$ that are contained in Ω (internal edges), while $\mathcal{T}_h^i$, $\mathcal{T}_h^o$ and $\mathcal{T}_h^w$ denote the sets of edges $\Gamma \in \mathcal{T}_h$ such that $\Gamma \subset \partial\Omega_i$, $\Gamma \subset \partial\Omega_o$ and $\Gamma \subset \partial\Omega_w$ respectively. Finally we define $\mathcal{T}_h^B = \mathcal{T}_h^o \cup \mathcal{T}_h^i \cup \mathcal{T}_h^w$ the set of all boundary edges.

Let us introduce the following space of discontinuous finite elements:

$$Y_h^r = \left\{ v_h \in L^2(\Omega) : v_h|_K \in \mathbb{P}_r,\ \forall K \in \mathcal{T}_h \right\}$$

where $\mathbb{P}_r$ denotes the space of polynomals of degree r.
Let $\boldsymbol{V_h} = Y_h^r \times [Y_h^r]^2 \times Y_h^r$ be a finite dimensional subspace of $\boldsymbol{V}$; the weak form of our problem has been stated in a semi-discrete form and so its finite element formulation reads as follows:
$\forall t > 0$, find $\boldsymbol{U_h}(t) \in \boldsymbol{V_h}$ such that:

$$\int_\Omega \frac{\partial \boldsymbol{U_h}}{\partial t} \cdot \boldsymbol{v_h}\, d\Omega = \int_\Omega \sum_{i=1}^{2} \boldsymbol{F_i} \cdot \frac{\partial \boldsymbol{v_h}}{\partial x_i}\, d\Omega - \int_{\partial\Omega} \boldsymbol{F_i} n_i \cdot \boldsymbol{v_h}, d\Gamma \qquad \forall \boldsymbol{v_h} \in \boldsymbol{Vh} \quad (3.1)$$

with $\boldsymbol{U_h}(0) = \boldsymbol{U_{0h}} \in \boldsymbol{V_h}$.
Here $\boldsymbol{U_{0h}}$ denotes the $\boldsymbol{V_h}$ projection of the function $\boldsymbol{U_0}$ from the initial condition.

By splitting the integrals over Ω appearing in equation (3.1) into the sum of integrals over the elements K we obtain a semi-discrete equation for a generic element K which can be written as

$$\int_K \frac{\partial \boldsymbol{U_h}}{\partial t} \cdot \boldsymbol{v_h} d\Omega = \int_K \sum_{i=1}^{2} \boldsymbol{F_i} \cdot \frac{\partial \boldsymbol{v_h}}{\partial x_i} \, d\Omega - \int_{\partial K} \sum_{i=1}^{2} \boldsymbol{F_i} n_i \cdot \boldsymbol{v_h} \, d\Gamma \quad \forall \boldsymbol{v_h} \quad (3.2)$$

where ∂K denotes the boundary of element K.

Due to the discontinuous function approximation, flux terms are not uniquely defined at element interfaces. It is at this stage that the technique traditionally used in finite volume schemes is borrowed by the discontinuous finite element method.
The crucial point of the discontinuous Galerkin approximation is the evaluation of the integral over ∂K and these integrals are computed with the aid of a numerical flux, also known as approximate Riemann solver, $\boldsymbol{H}$; in order to expalin it clearly we need to introduce some notation: for two adjacent elements K^+ and K^- of the triangulation T_h and a point $\boldsymbol{x}$ of their common boundary at which the outward unitary normals $\boldsymbol{n}^\pm$ are well defined, we set

$$\boldsymbol{U}_{\boldsymbol{h}}^{\pm}(\boldsymbol{x}) = \lim_{\epsilon \to 0^+} \boldsymbol{U_h}(\boldsymbol{x} - \epsilon \boldsymbol{n}^{\pm})$$

and we call these values the traces of $\boldsymbol{U_h}$ from the interior of $K^\pm$. Moreover we define mean $\{\cdot\}$ and jump $[\cdot]$ values by:

$$\{\boldsymbol{U_h}\} = \frac{1}{2}\left(\boldsymbol{U}_{\boldsymbol{h}}^{+} + \boldsymbol{U}_{\boldsymbol{h}}^{-}\right)$$
$$[\boldsymbol{U_h}] = \boldsymbol{U}_{\boldsymbol{h}}^{+} - \boldsymbol{U}_{\boldsymbol{h}}^{-}$$

We underline that the value of $[\boldsymbol{U_h}]$ depends on the orientation of the outward unitary normal $\boldsymbol{n}$, while $[\boldsymbol{U_h}] \cdot \boldsymbol{n}$ is independent on this orientation.

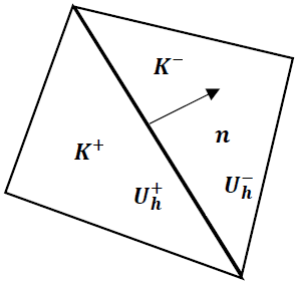

Figure 1: Interior face and orientation

The numerical flux has to satisfy a *conservativity* condition, namely

$$\boldsymbol{H}(\boldsymbol{U}_{\boldsymbol{h}}^{-}(\boldsymbol{x}), \boldsymbol{U}_{\boldsymbol{h}}^{+}(\boldsymbol{x}), \boldsymbol{n}^{+}) + \boldsymbol{H}(\boldsymbol{U}_{\boldsymbol{h}}^{+}(\boldsymbol{x}), \boldsymbol{U}_{\boldsymbol{h}}^{-}(\boldsymbol{x}), \boldsymbol{n}^{-}) = 0$$

and a *consistency* condition, i.e. that

$$\boldsymbol{H}(\boldsymbol{U}(\boldsymbol{x}),\boldsymbol{U}(\boldsymbol{x}),\boldsymbol{n}) = \sum_{i=1}^{2} \boldsymbol{F_i} n_i$$

The main examples of numerical fluxes satisfying all the above requirements are reported in [1]. In this case, and more in general when we deal with multidimensional systems, a good choice is represented by local Lax-Friedrichs (Rusanov) flux because it can be easily applied to any non-linear hyperbolic system, it is simple to compute, and yields good results;its expression is the following:

$$\boldsymbol{H}(\boldsymbol{U_h^-}(\boldsymbol{x}),\boldsymbol{U_h^+}(\boldsymbol{x}),\boldsymbol{n}) = \sum_{i=1}^{2} \{\boldsymbol{F_i}\} n_i + \frac{C}{2} [\boldsymbol{U_h}]$$

where C is larger than the largest eigenvalue (in absolute value) of the Jacobian matrix $\frac{\partial \boldsymbol{F}(\boldsymbol{U_h^\pm})}{\partial \boldsymbol{U}} \cdot \boldsymbol{n}^\pm$.

If we plug the numerical flux in the boundary integral in (3.2) and we sum up over all elements we find:

$$\begin{aligned} &\sum_{K\in\mathcal{T}_h} \int_K \frac{\partial \boldsymbol{U_h}}{\partial t} \cdot \boldsymbol{v_h} d\Omega = \sum_{K\in\mathcal{T}_h} \int_K \sum_{i=1}^{2} \boldsymbol{F_i} \cdot \frac{\partial \boldsymbol{v_h}}{\partial x_i} d\Omega \\ &- \sum_{K\in\mathcal{T}_h} \int_{\partial K} \boldsymbol{H}(\boldsymbol{U_h^-}(\boldsymbol{x}),\boldsymbol{U_h^+}(\boldsymbol{x}),\boldsymbol{n}) \cdot \boldsymbol{v_h} \qquad \forall \boldsymbol{v_h} \in \boldsymbol{V_h} \end{aligned} \tag{3.3}$$

We notice that in the sum over all elements each edge Γ between neighboring K^+ and K^- occurs twice with opposite outward unitary normals and states. The sum of boundary integrals into (3.3) can be separated into the sum of the contribution due to the inner edges and the one due to the boundary edges; indeed if we consider an internal edge Γ shared by the elements K^+ with outward unitary normal $\boldsymbol{n}^+$ and K^- with outward unitary normal $\boldsymbol{n}^-$ we find:

$$\int_\Gamma \boldsymbol{H}(\boldsymbol{U_h^-}(\boldsymbol{x}),\boldsymbol{U_h^+}(\boldsymbol{x}),\boldsymbol{n}^+) \cdot \boldsymbol{v_h^+} d\Gamma + \int_\Gamma \boldsymbol{H}(\boldsymbol{U_h^+}(\boldsymbol{x}),\boldsymbol{U_h^-}(\boldsymbol{x}),\boldsymbol{n}^-) \cdot \boldsymbol{v_h^-} d\Gamma =$$

$$\int_\Gamma \boldsymbol{H}(\boldsymbol{U_h^-}(\boldsymbol{x}),\boldsymbol{U_h^+}(\boldsymbol{x}),\boldsymbol{n}^+) \cdot \boldsymbol{v_h^+} d\Gamma - \int_\Gamma \boldsymbol{H}(\boldsymbol{U_h^-}(\boldsymbol{x}),\boldsymbol{U_h^+}(\boldsymbol{x}),\boldsymbol{n}^+) \cdot \boldsymbol{v_h^-} d\Gamma =$$

$$\int_\Gamma \boldsymbol{H}(\boldsymbol{U_h^-}(\boldsymbol{x}),\boldsymbol{U_h^+}(\boldsymbol{x}),\boldsymbol{n}^+) \cdot [\boldsymbol{v_h}] d\Gamma$$

thanks to conservativity condition.
Therefore we get the following equivalent formulation:

$$\begin{aligned}
&\sum_{K\in\mathcal{T}_h}\int_K \frac{\partial \boldsymbol{U_h}}{\partial t}\cdot \boldsymbol{v_h} d\Omega = \sum_{K\in\mathcal{T}_h}\int_K \sum_{i=1}^{2} \boldsymbol{F_i}\cdot\frac{\partial \boldsymbol{v_h}}{\partial x_i}\, d\Omega \\
&-\sum_{\Gamma\in\mathcal{T}_h^I}\int_\Gamma \boldsymbol{H}(\boldsymbol{U_h^-},\boldsymbol{U_h^+},\boldsymbol{n})\cdot[\boldsymbol{v_h}]\; d\Gamma \\
&-\sum_{\Gamma\in\mathcal{T}_h^B}\int_\Gamma \boldsymbol{H}(\boldsymbol{U_h^-},\boldsymbol{U_h^+},\boldsymbol{n})\cdot \boldsymbol{v_h}\, d\Gamma \qquad \forall \boldsymbol{v_h}\in\boldsymbol{V_h}
\end{aligned} \tag{3.4}$$

The relation (3.4) can be expressed in the following manner:

$$\frac{d}{dt}\left(\boldsymbol{U_h},\boldsymbol{v_h}\right) = \boldsymbol{b_h}\left(\boldsymbol{U_h},\boldsymbol{v_h}\right) \quad \forall \boldsymbol{v_h}\in\boldsymbol{V_h} \tag{3.5}$$

where

$$\left(\boldsymbol{U_h},\boldsymbol{v_h}\right) = \sum_{K\in\mathcal{T}_h}\int_K \frac{\partial \boldsymbol{U_h}}{\partial t}\cdot\boldsymbol{v_h} d\Omega = \int_\Omega \frac{\partial \boldsymbol{U_h}}{\partial t}\cdot\boldsymbol{v_h} d\Omega$$

$$\begin{aligned}
\boldsymbol{b_h}\left(\boldsymbol{U_h},\boldsymbol{v_h}\right) = &\sum_{K\in\mathcal{T}_h}\int_K \sum_{i=1}^{2}\boldsymbol{F_i}\cdot\frac{\partial \boldsymbol{v_h}}{\partial x_i}\, d\Omega - \sum_{\Gamma\in\mathcal{T}_h^I}\int_\Gamma \boldsymbol{H}(\boldsymbol{U_h^-},\boldsymbol{U_h^+},\boldsymbol{n})\cdot[\boldsymbol{v_h}]\; d\Gamma \\
&-\sum_{\Gamma\in\mathcal{T}_h^B}\int_\Gamma \boldsymbol{H}(\boldsymbol{U_h^-},\boldsymbol{U_h^+},\boldsymbol{n})\cdot\boldsymbol{v_h}\, d\Gamma \quad \forall \boldsymbol{v_h}\in\boldsymbol{V_h}
\end{aligned}$$

3.1. Treatment of boundary conditions

We recall that the boundary $\mathcal{T}_h^B = \mathcal{T}_h^w \cup \mathcal{T}_h^i \cup \mathcal{T}_h^o$. For $\Gamma \in \mathcal{T}_h^B$ we should replace the value $\boldsymbol{U_h^-}$ with a suitable boundary function $\boldsymbol{U_\Gamma}(\boldsymbol{U_h^+})$.

Let us analyse first impermeability condition, i.e. $\boldsymbol{u}\cdot\boldsymbol{n} = 0$ where $\boldsymbol{u}$ is the velocity vector and $\boldsymbol{n}$ is the outward unitary normal with respect to $\partial\Omega_w$ which involves the edges that belong to $\mathcal{T}_h^w$: this condition has to be incorporated is some way into the expression of $\boldsymbol{H}(\boldsymbol{U_h^-},\boldsymbol{U_h^+},\boldsymbol{n})$ that appears in the definition of the form $\boldsymbol{b_h}(\boldsymbol{U_h},\boldsymbol{v_h})$ and a natural way is the strong (direct) imposition in the physical flux. This implies that

$$\sum_{i=1}^{2}\boldsymbol{F_i} n_i = (0, pn_1, pn_2, 0)^T := \boldsymbol{f_w}$$

and therefore

$$\sum_{\Gamma\in\mathcal{T}_h^W}\int_\Gamma \boldsymbol{H}(\boldsymbol{U_h^-},\boldsymbol{U_h^+},\boldsymbol{n})\cdot\boldsymbol{v_h}\, d\Gamma = \sum_{\Gamma\in\mathcal{T}_h^w}\int_\Gamma \boldsymbol{f_w}\cdot\boldsymbol{v_h} d\Gamma$$

Let us analyse now the conditions for the inlet and the outlet part of the boundary; the right choice depends on the sign of the eigenvalues of the Jacobian matrix and, as reported in [8], it can be shown that the eigenvalues of this matrix are

$$\lambda_1 = \boldsymbol{u} \cdot \boldsymbol{n} - c$$
$$\lambda_2 = \lambda_3 = \boldsymbol{u} \cdot \boldsymbol{n}$$
$$\lambda_4 = \boldsymbol{u} \cdot \boldsymbol{n} + c$$

Now we can distinguish four cases:

1. $\lambda_i < 0, i = 1...4$ which corresponds to a supersonic inflow where we impose Dirichlet boundary conditions, namely $\boldsymbol{U_\Gamma}(\boldsymbol{U}) = \boldsymbol{U_\infty}$, where $\boldsymbol{U_\infty}$ is the free-stream value of the conserved variables

$$\boldsymbol{U_\infty} = (\rho_\infty, \rho_\infty u_{1,\infty}, \rho_\infty u_{2,\infty}, (\rho E)_\infty)^T$$

2. $\lambda_i < 0, i = 1...3$ and $\lambda_4 > 0$ which corresponds to a subsonic inflow where we take the pressure from the flow field and we impose all other variables based on free-stream conditions, namely

$$\boldsymbol{U_\Gamma}(\boldsymbol{U}) = \left(\rho_\infty, \rho_\infty u_{1,\infty}, \rho_\infty u_{2,\infty}, \frac{p}{\gamma - 1} + \rho_\infty (u_{1,\infty}^2 + u_{2,\infty}^2)\right)^T$$

   where p is computed with the constitutive equation of ideal gases.

3. $\lambda_i > 0, i = 1...4$ which corresponds to a supersonic outflow and we take the values from the computed variables, namely $\boldsymbol{U_\Gamma}(\boldsymbol{U}) = \boldsymbol{U}$

4. $\lambda_1 < 0$ and $\lambda_i > 0, i = 2...4$ which corresponds to a subsonic outflow where we impose an outflow pressure p_{out} and we take all other variables from the flow field, namely:

$$\boldsymbol{U_\Gamma}(\boldsymbol{U}) = \left(U_1, U_2, U_3, \frac{p_{out}}{\gamma - 1} + \frac{U_2^2 + U_3^2}{2U_1}\right)^T$$

   where $U_i, i = 1..3$ is the i-th component of the vector $\boldsymbol{U}$ and they correspond to the density and the momentum along x_1 and x_2 direction respectively.

Another possibility is to apply characteristic far-field boundary conditions that impose Dirichlet conditions based on free-stream conditions on characteristic inflow variables, while no boundary conditions are imposed on characteristic outflow variables.

Summing up according to the specific problem we modify the term $\boldsymbol{H}(\boldsymbol{U_h^-}, \boldsymbol{U_h^+}, \boldsymbol{n})$ for $\Gamma \in \mathcal{T}_h^i \cup \mathcal{T}_h^o$ in order to take into account the physical properties of the flow.

3.2. Shock capturing

In high-order numerical methods applied to the solution of high speed flows with shock waves and contact discontinuities we can observe the Gibbs phenomenon manifested by spurious (non physical) oscillations in computed quantities propagating from discontinuities; in DG numerical solutions the Gibbs phenomenon is manifested by spurious overshoots and undershoots in the vicinity of discontinuities.
In order to correct this undesirable feature, in the framework of finite volume methods, one uses suitable limiting procedures: they should preserve the high-order accuracy of the method in regions where the solution is regular, and decrease the order to 1 in a neighbourhood of discontinuities or steep gradients. These methods are based on the use of the flux limiter.
Another possibility, the one that we will use, is more typical of the finite elements framework and it is based on the concept of artificial viscosity applied locally on the basis of a suitable *jump* indicator.

As reported in [4], numerical experiments and simulations show that interelement jumps in the approximate solution, for a suitable choice of polynomial degree and numerical method, are on the interior faces Γ $[\boldsymbol{U_h}]_\Gamma = O(1)$, but $[\boldsymbol{U_h}]_\Gamma = O(h^{k+1})$ where the solution is smooth.
First part of our approach is therefore the introduction of this *jump* indicator proposed in [5] to evaluate the inter-element jumps of the approximate solution and defined by

$$g_K(\boldsymbol{U_h}) = \int_{\partial K} \frac{[\rho_h]^2}{\left(h_K \left|K\right|^{3/4}\right)} d\Gamma, \qquad K \in T_h$$

where ρ_h is the density corresponding to the state $\boldsymbol{U_h}$ and $|K|$ is the measure of the element K.
The indicator g_K was constructed in such a way that it takes an anisotropy of the computational mesh into account and it was shown in [5] that it identifies discontinuities safely on unstructured and anisotropic meshes.
Now we introduce the discrete *jump* indicator:

$$G_K(\boldsymbol{U_h}) = \begin{cases} 0 & \text{if } g_K(\boldsymbol{U_h}) < \xi_{min} \\ \frac{1}{2}\sin\left(\pi \frac{g_K(\boldsymbol{U_h}) - (\xi_{max} - \xi_{min})}{2(\xi_{max} - \xi_{min})}\right) + \frac{1}{2} & \text{if } \xi_{min} \le g_K(\boldsymbol{U_h}) < \xi_{max} \\ 1 & \text{if } g_K(\boldsymbol{U_h}) \ge \xi_{max} \end{cases}$$

where $0 \le \xi_{min} < \xi_{max}$. In practical applications, it is suitable to set $\xi_{min} = 0.5$ and $\xi_{max} = 1.5$.

On the basis of the discrete *jump* indicator we introduce local artificial viscosity forms, which are included in the numerical schemes for solving

inviscid compressible flow. We define the artificial viscosity forms $\boldsymbol{\beta_h}$: $\boldsymbol{V_h} \times \boldsymbol{V_h} \times \boldsymbol{V_h} \to \mathbb{R}$ and $\boldsymbol{\gamma_h} : \boldsymbol{V_h} \times \boldsymbol{V_h} \times \boldsymbol{V_h} \to \mathbb{R}$

$$\boldsymbol{\beta_h}(\bar{\boldsymbol{w}}_{\boldsymbol{h}}, \boldsymbol{w_h}, \boldsymbol{\varphi_h}) = \nu_1 \sum_{K \in T_h} h_K G_K(\bar{\boldsymbol{w}}_{\boldsymbol{h}}) \int_K \nabla \boldsymbol{w_h} : \nabla \boldsymbol{\varphi_h} d\Omega$$

and

$$\boldsymbol{\gamma_h}(\bar{\boldsymbol{w}}_{\boldsymbol{h}}, \boldsymbol{w_h}, \boldsymbol{\varphi_h}) = \nu_2 \sum_{K \in T_h^I} \frac{1}{2} \left(G_{K_\Gamma}^{(L)}(\bar{\boldsymbol{w}}_{\boldsymbol{h}}) + G_{K_\Gamma}^{(R)}(\bar{\boldsymbol{w}}_{\boldsymbol{h}}) \right) \int_K [\boldsymbol{w_h}] \cdot [\boldsymbol{\varphi_h}] \, d\Omega$$

with $\nu_1 = O(1)$ and $\nu_2 = O(1)$ positive constants.
Here $K_\Gamma^{(L)}$ and $K_\Gamma^{(R)} \in T_h$ denote the elements sharing the inner edge $\Gamma \in T_h^I$.

A fundamental characteristic of this approach is that G_K vanishes in regions where the solution is regular and therefore the scheme does not produce any non physical entropy in these regions.
The artificial viscosity forms $\boldsymbol{\beta_h}$ and $\boldsymbol{\gamma_h}$ are added to semi-discrete formulation and so we get: $\forall t > 0$ find $\boldsymbol{U_h}(t) \in \boldsymbol{V_h}$ such that

$$\frac{d}{dt} (\boldsymbol{U_h}, \boldsymbol{v_h}) + \boldsymbol{b_h}(\boldsymbol{U_h}, \boldsymbol{v_h}) + \boldsymbol{\beta_h}(\boldsymbol{U_h}, \boldsymbol{U_h}, \boldsymbol{v_h}) + \boldsymbol{\gamma_h}(\boldsymbol{U_h}, \boldsymbol{U_h}, \boldsymbol{v_h}) = 0 \quad \forall \boldsymbol{v_h} \in \boldsymbol{V_h} \tag{3.6}$$

with $\boldsymbol{U_h}(0) = \boldsymbol{U_{0_h}}$.

The functions $\boldsymbol{U_h}$ and $\boldsymbol{v_h}$ can be expressed as linear combination of n shape functions ϕ_i,

$$\boldsymbol{U_h} = \sum_{i=1}^{n} \boldsymbol{U_i}(t) \phi_i(\boldsymbol{x})$$
$$\boldsymbol{v_h} = \sum_{i=1}^{n} \boldsymbol{v_i} \phi_i(\boldsymbol{x})$$

where $\boldsymbol{U_i}(t)$ and $\boldsymbol{v_i}$ denote the degrees of freedom of the numerical solution and of the test function for an element K; therefore equation (3.6) is equivalent to a system of n equations.

We find therefore the system of ordinary differential equations:

$$M \frac{d}{dt} \boldsymbol{U_h} = \tilde{L_h}(\boldsymbol{U_h}) \tag{3.7}$$

We finally underline that the mass matrix M is block-diagonal and so it is easily invertible; thus we can rewrite the system (3.7) as

$$\frac{d}{dt} \boldsymbol{U_h} = L_h(\boldsymbol{U_h}) \tag{3.8}$$

3.3. Convergence analysis

The theoretical analysis of the described approach has been carried out in [9], where the authors proved the convergence of the discontinuous Galerkin finite element method with polynomials of arbitrary degree $p \geq 0$ on general unstructured meshes.

The proof is based on providing convergence of a sequence of approximate solutions satisfying the following three conditions:

1. uniform bound in $L_\infty((0,T);L_2(\Omega))$, i.e. L_∞ in time and L_2 in space.
2. consistency with all entropies inequalities
3. consistency with initial data.

If we denote by U_{h_j} the components of the vector $\boldsymbol{U_h}$ and by F_{1_j} and F_{2_j} the components of the convective flux $\boldsymbol{F} = (\boldsymbol{F_1}, \boldsymbol{F_2})$ we recall that in general $\boldsymbol{U_h} \in [L^\infty(\mathbb{R}_+; L^2(\mathbb{R}^2)) \cap L^\infty(\mathbb{R}_+; L^2(\mathbb{R}^2))]^4$ is an entropic solution if

1. for all Kruzkov entropy pairs $(\eta_j, q_{1_j}, q_{2_j})$ with $\eta_j(x) = |x-k| \, \forall k \in \mathbb{R}$ and associated entropy fluxes $q_{i_j}(x) = \text{sign}\,(x-k)(F_{i_j}(x) - F_{i_j}(k)$ related through the compatibility condition

$$q'_{i_j} = F'_{i_j} \eta'_j, \qquad i = 1,2$$

   U_{h_j} satisfies in the distributional sense the inequality

$$\frac{\partial \eta_j(U_{h_j})}{\partial t} + \sum_{i=1}^{2} \frac{\partial q_{i_j}(U_{h_j})}{\partial x_i} \leq 0 \qquad \forall j = 1,..,4$$

2. $\boldsymbol{U_h}$ satisfies the initial condition in the following sense

$$\lim_{t \to 0^+} \|\boldsymbol{U_h}(\boldsymbol{\cdot}, \boldsymbol{t}) - \boldsymbol{U_0}\|_{L^1} = 0$$

The key point of the analysis is the proof of the so-called Kruzkov entropy condition: for all Kruzkov entropies $\eta_j(\lambda) = |\lambda - k|$ with $k \in \mathbb{R}$ and $0 \leq \phi \in C_0^\infty(\Omega)$, we have

$$\limsup_{h \to 0} - \int_0^T \int_\Omega q_j(U_{h_j}) \cdot \nabla \phi d\Omega dt \leq 0 \qquad j = 1,...,4$$

where $q_j = (\eta_j, q_{1_j}, q_{2_j})^T$ where $q_{i_j}, \quad i = 1,2$ is the entropy flux satisfying the compatibility condition introduce above.

Eventually in the case $p = 0$ the following *a posteriori* error estimate has been proven

$$\|\boldsymbol{U} - \boldsymbol{U_h}\|_{L^2((0,T);L^2(\Omega))} \leq C \, \|h^\alpha R(\boldsymbol{U_h})\|_{L^2((0,T);L^2(\Omega))}$$

where for an elements K we have

$$\begin{aligned} R(\boldsymbol{U_h})|_K = &\max_K |\nabla \cdot \boldsymbol{F}(\boldsymbol{U_h})| + \max_{\partial K, \partial K \not\subset T_h^B} |[\boldsymbol{F}(\boldsymbol{U_h})] \cdot \boldsymbol{n}| \, / h_K \\ &+ \lambda \max_{\partial K, \partial K \not\subset T_h^B} |[\boldsymbol{U_h}]| \, / h_K \end{aligned}$$

and $\frac{1}{2} \leq \alpha \leq 1$.
Typically $\alpha = \frac{1}{2}$ where the solution is smooth and $\alpha = 1$ in the presence of a shock.

4. Time discretization

The semidiscrete problem (3.8) found in the previous section represents a system of ordinary differential equations (ODEs) which has to be solved with the aid of suitable numerical schemes. Since one of the reasons for employing discontinuous Galerkin finite elements is to achieve high-order accuracy, when high-order degrees polynomials are used a high-order Runge-Kutta (RK) method that matches the accuracy of the space discretization has to be used: the combination of discontinuous Galerkin finite elements and Runge-Kutta scheme leads to the so called RKDG (Runge-Kutta Discontinuous Galerkin) method.
We discretize in time our system of ordinary differential equations by using the following RK method of order m:

1. Set $\boldsymbol{U_h^{(0)} = U_h^n}$
2. For $i = 1, 2, ..., m$ compute the intermediate functions:

$$\boldsymbol{U_h^{(i)}} = \sum_{l=0}^{i-1} \alpha_{il} \boldsymbol{w_h^{il}}, \qquad \boldsymbol{w_h^{il}} = \boldsymbol{U_h^{(l)}} + \frac{\beta_{il}}{\alpha_{il}} \Delta t^n L_h(\boldsymbol{U_h^{(l)}})$$

   where Δt^n is the time-step to compute $\boldsymbol{U_h^{n+1}}$
3. Set $\boldsymbol{U_h^{n+1} = U_h^{(m)}}$

which is required to to satisfy the following conditions:

a) If $\beta_{il} \neq 0$ then $\alpha_{il} \neq 0$

b) $\alpha_{il} \geq 0$

c) $\sum_{l=0}^{i-1} \alpha_{il} = 1$

The distinctive feature of these RK methods is that their stability follows from the stability of the mapping $\boldsymbol{U_h^{(l)}} \mapsto \boldsymbol{w_h^{il}}$ defining the intermediate steps. Indeed, if we assume that, for some arbitrary semi-norm $|\cdot|$, we have

that $\left|\boldsymbol{w_h^{il}}\right| \leq \left|\boldsymbol{U_h^{(l)}}\right|$, then:

$$\begin{aligned}
\left|\boldsymbol{U_h^{(i)}}\right| &= \left|\sum_{l=0}^{i-1} \alpha_{il} \boldsymbol{w_h^{il}}\right| \\
&\leq \sum_{l=0}^{i-1} \alpha_{il} \left|\boldsymbol{w_h^{il}}\right| \quad \text{by positivity property (b)} \\
&\leq \sum_{l=0}^{i-1} \alpha_{il} \left|\boldsymbol{U_h^{(l)}}\right| \quad \text{by stability assumption} \\
&\leq \max_{0\leq l\leq i-1} \left|\boldsymbol{U_h^{(l)}}\right| \quad \text{by consistency property (c)}
\end{aligned}$$

It is clear now that the inequality $\left|\boldsymbol{U_h^n}\right| \leq \left|\boldsymbol{U_{0h}}\right|, \forall n \geq 0$ follows frome the above inequality by simple inductions argument.

The classical RK is simple and widely used but it has the disadvantage that it requires m extra storages for the intermediate functions. An attractive alternative to this is a low-storage version (LSRK) which requires only one additional storage level.
For the sake of clarity we report the coefficients and the expression used for the low-storage of fourth-order RK method as stated in [6].

i	a_i	b_i
1	0	$\frac{1432997174477}{9575080441755}$
2	$-\frac{567301805773}{1357537059087}$	$\frac{5161836677717}{13612068292357}$
3	$-\frac{2404267990393}{2016746695238}$	$\frac{1720146321549}{2090206949498}$
4	$-\frac{3550918686646}{2091501179385}$	$\frac{3134564353537}{4481467310338}$
5	$-\frac{1275806237668}{842570457699}$	$\frac{2277821191437}{14882151754819}$

Figure 2: Coefficients for the low-storage fourth-order RK method

1. Set $\boldsymbol{U_h^{(0)}} = \boldsymbol{U_h^n}, \boldsymbol{w_h^{(0)}} = \mathbf{0}$
2. For $i \in [1, 5]$ compute the intermediate steps:

$$\boldsymbol{w_h^{(i)}} = a_i \boldsymbol{w_h^{(i-1)}} + \Delta t^n L_h \left(\boldsymbol{U_h^{(i-1)}} \right)$$

$$\boldsymbol{U_h^{(i)}} = \boldsymbol{U_h^{(i-1)}} + b_i \boldsymbol{w_h^{(i)}}$$

   where Δt^n is the time-step to compute $\boldsymbol{U_h^{n+1}}$
3. Set $\boldsymbol{U_h^{n+1}} = \boldsymbol{U_h^{(5)}}$

The main disadvantage with respect to the classical RK method is an additional function evaluation but this is well balanced by the fact that the memory usage is significantly reduced.

As any explicit method, also RKDG scheme must satisfy a CFL(Courant-Friedrichs-Lewy) condition to achieve convergence written,for example, in the form

$$\Delta t \leq \text{CFL} \min_{K \in T_h, \Gamma \subset \partial K} \frac{|K|}{\lambda |\Gamma|}$$

where $|K|$ is the area of the element K and $|\Gamma|$ is the length of the corresponding edge.

Cockburn and Sun in [1] found that using polynomial of degree k and a $k+1$ RK method (which give rise to an $(k+1)$th order accurate method) we can take in practice a Courant number less or equal than $\frac{1}{2k+1}$.
Indeed this can be proven for $k = 0$ and for $k = 1$; moreover if $k \geq 2$ the number $\frac{1}{2k+1}$ is less than 5% smaller than limiting values for Courant number numerically-obtained. In Figure 2 we display this estimates for a wide variety of time and space discretizations (the symbol $\star$ indicates that the method is unstable when the ratio $\Delta t/h$ is held constant).

k	0	1	2	3	4	5	6	7	8
$\nu = 1$	1.000	★	★	★	★	★	★	★	★
$\nu = 2$	1.000	0.333	★	★	★	★	★	★	★
$\nu = 3$	1.256	0.409	0.209	0.130	0.089	0.066	0.051	0.040	0.033
$\nu = 4$	1.392	0.464	0.235	0.145	0.100	0.073	0.056	0.045	0.037
$\nu = 5$	1.608	0.534	0.271	0.167	0.115	0.085	0.065	0.052	0.042
$\nu = 6$	1.776	0.592	0.300	0.185	0.127	0.093	0.072	0.057	0.047
$\nu = 7$	1.977	0.659	0.333	0.206	0.142	0.104	0.080	0.064	0.052
$\nu = 8$	2.156	0.718	0.364	0.225	0.154	0.114	0.087	0.070	0.057
$\nu = 9$	2.350	0.783	0.396	0.245	0.168	0.124	0.095	0.076	0.062
$\nu = 10$	2.534	0.844	0.428	0.264	0.182	0.134	0.103	0.082	0.067
$\nu = 11$	2.725	0.908	0.460	0.284	0.195	0.144	0.111	0.088	0.072
$\nu = 12$	2.911	0.970	0.491	0.303	0.209	0.153	0.118	0.094	0.077

Figure 3: CFL numbers for polynomials of degree k and RK methods of order ν (taken from [1])

Eventually we underline that the integrals in (3.3) need to be approximated by quadrature rules; in [1] it has been shown that, using finite element spaces of order k, if the quadrature rules over each of the faces of the border of the element K are exact for polynomials of degree $2k+1$ and and if the one over the element is exact for polynomials of degree $2k$ the following estimate holds:

$$\|\boldsymbol{L_h}(\boldsymbol{U}) + \nabla \cdot \boldsymbol{F}(\boldsymbol{U})\|_{L^\infty(K)} \leq Ch^{k+1} \, |\boldsymbol{F}(\boldsymbol{U})|_{W^{k+2,\infty}(K)}$$

where $|\cdot|_{W^{k+2,\infty}(K)}$ is a seminorm in the following space

$$W^{k+2,\infty}(K) = \{f \in L^\infty(K) | D^\alpha f \in L^\infty(K) \quad \forall \alpha \leq k+2\}$$

namely the space of essentially bounded function in the element K such that each weak derivative up to order $k+2$ is essentially bounded in K.

5. Numerical example: supersonic flow over a double wedge airfoil

In this section we present the solution of a test problem in order to show the performance of the technique introduced above; the scheme has been implemented in FREEFEM++.

We consider supersonic inviscid flow over a double-wedge airfoil in a thermally ideal gas with different far-field Mach numbers (the ratio between the flow velocity and the speed velocity in the fluid), different angles of attack (the angle between the chord of the airfoil and the direction of the incoming velocity)α, a far-field density $\rho_\infty = 1.2 \quad \mathrm{kg/m^3}$ which corresponds to the air density at 300 K and a far-field pressure $p_\infty = 1$ atm $= 101325$ Pa.
We seek the steady-state solution of the Euler equations with the use of an unstructured triangular grid and employing P_0 polynomials with a second order strong stability preserving (SSP) Runge-Kutta method in order to easily test the proposed technique.

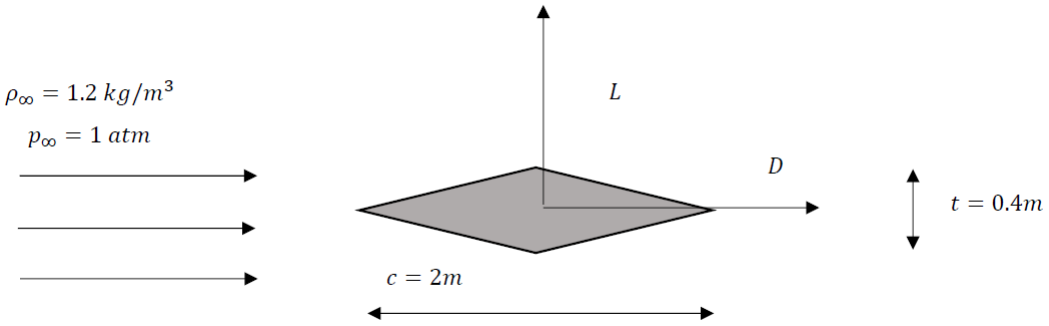

Figure 4: Schematic diagram of the geometry of the airfoil

Before starting we recall some concepts: a shock wave is a type of propagating disturbance; when a wave moves faster than the local speed of sound in a fluid, it is a shock wave. Like a classical wave it carries energy and can propagate through a medium, but it is characterized by a sudden (nearly discontinuous) change in pressure and density in the medium. Moreover in a supersonic flow that turns around a corner additional increased expansion is achieved through an expansion fan, technically known as Prandtl-Mayer expansion fan.

Let us briefly introduce some theoretical aspects: a concave corner generates an oblique shock (compression), while a convex corner generates an expansion fan and therefore the flow regime under consideration leads to two shock waves and an expansion wave.

The flow quantities change across an oblique shock and across an expansion fan are in opposite direction as reported in Figure 5.

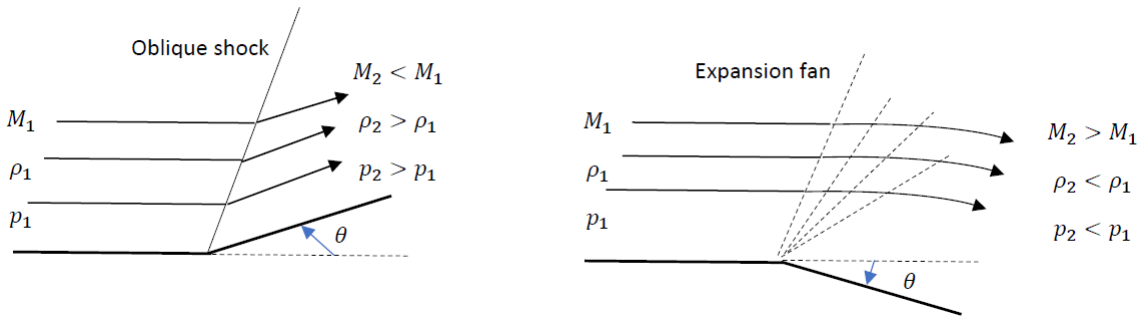

Figure 5: Comparison between compression and expansion waves

Let us analyse more in detail the oblique shock wave; using a control volume analysis we can derive the relations between the components of density, pressure and velocity before and after the compression wave. As reported in Figure 6 velocity components are taken in coordinates normal and tangent to the shock; the upstream flow components are

$$V_{1n} = V_1 \sin\beta$$
$$V_{1t} = V_1 \cos\beta$$

where β is the shock wave angle as reported in Figure 6.

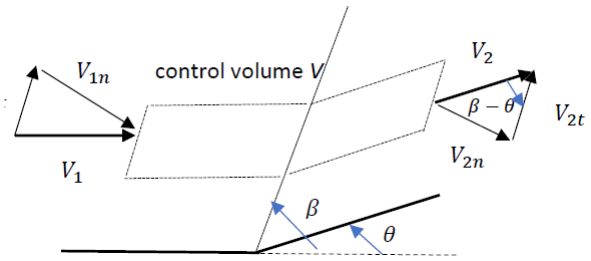

Figure 6: Control volume analysis

If we apply continuity equation to the control volume V we find

$$\int_V \nabla \cdot (\rho \boldsymbol{V})\, dV = -\int_{\partial V} \rho \boldsymbol{V} \cdot \boldsymbol{n} dA = 0$$

which implies

$$\rho_1 V_{1n} = \rho_2 V_{2n}.$$

Similar relations can be obtained using other conservation laws and in particular it is easy to find, using momentum equation in tangential direction, that $V_{1t} = V_{2t}$.

Before deriving a relation between the two angles β and θ we need to employee in a suitable manner well known relations in the case of normal shock wave: we define the normal Mach numbers as

$$M_{1n} = M_1 \sin\beta$$
$$M_{2n} = M_1 \sin(\beta - \theta)$$

and the static properties ratios can be obtained using the normal-shock relations; in particular

$$\frac{\rho_2}{\rho_1} = \frac{(\gamma+1)M_{1n}^2}{2+(\gamma-1)M_{1n}^2}$$
$$\frac{p_2}{p_1} = 1 + \frac{2\gamma}{\gamma+1}(M_{1n}^2 - 1)$$

Now we can use these relation to compute the wave angle β: indeed we have

$$\tan(\beta - \theta) = \frac{V_{2n}}{V_{2t}}$$
$$\tan\beta = \frac{V_{1n}}{V_{1t}}$$

which implies

$$\frac{\tan(\beta-\theta)}{\tan\beta} = \frac{V_{2n}}{V_{2t}}\frac{V_{1t}}{V_{1n}} = \frac{V_{2n}}{V_{1n}} = \frac{\rho_1}{\rho_2} = \frac{2+(\gamma-1)M_{1n}^2}{(\gamma+1)M_{1n}^2}$$

Solving for θ we find

$$\tan\theta = \frac{2}{\tan\beta}\frac{M_1^2\sin\beta^2 - 1}{M_1^2(\gamma + 2\cos\beta) + 2} \tag{5.1}$$

which is an implicit definition of the function $\theta(\beta, M_1)$.
A graphical analysis of this function shows some interesting features; in Figure 7 we report the oblique shock chart and we notice that:

1. There is a maximum turning angle θ_{max} for any given upstream Mach number M_1; if the wall exceeds this ($\theta > \theta_{max}$) no oblique shock is possible and, instead, a detached shock forms ahead of the concave corner.

2. If $\theta < \theta_{max}$ two distinct oblique shocks with two different β angles are possible: the smaller β case is called *weak shock* and it is the most likely to happen in a supersonic flow, while the other case is called *strong shock* and it is unlikely to form over a straight-wall wedge

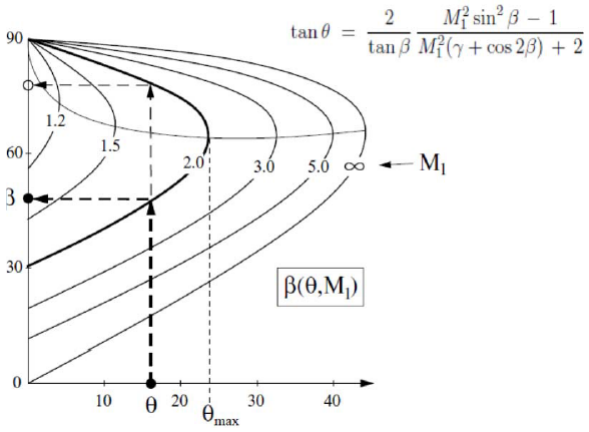

Figure 7: Oblique shock chart

Let us analyse now the features of the expansion fan: it can be considered as a continuous sequence of waves that turn the flow gradually (Mach waves). Across each Mach wave of the fan the flow direction changes by $d\theta$, while the velocity changes by dV and it can be shown that relation between these two quantities is

$$d\theta = \sqrt{M^2 - 1}\frac{dV}{V}$$

which can be rewritten in an equivalent form as

$$d\theta = \frac{\sqrt{M^2 - 1}}{1 + \frac{\gamma-1}{2}M^2}\frac{dM}{M}$$

as demonstrated in [10]. If we integrate the previous equation between two angle θ_1 and θ_2 we find

$$\theta_2 - \theta_1 = \nu(M_2) - \nu(M_1)$$

where

$$\nu(M) = \sqrt{\frac{\gamma+1}{\gamma-1}}\arctan\left(\sqrt{\frac{\gamma+1}{\gamma-1}}(M^2-1)\right) - \arctan\left(\sqrt{M^2-1}\right)$$

is known as Prandtl-Mayer function.

Another purpose of this simulation is to catch the correct behaviour of the main aerodynamic coefficients used to describe important parameters such as lift and drag; we consider the following adimensional coefficients:
the pressure coefficient C_p, the drag coefficient C_D and the lift coefficient

C_L defined as

$$C_p = \frac{p - p_\infty}{\frac{1}{2}\rho_\infty U_\infty^2}$$
$$C_D = \frac{D}{\frac{1}{2}\rho_\infty U_\infty^2 tc}$$
$$C_L = \frac{L}{\frac{1}{2}\rho_\infty U_\infty^2 tc}$$

Here U_∞ denotes the down-stream incoming velocity computed as $U_\infty = M_\infty \sqrt{\frac{\gamma p_\infty}{\rho_\infty}}$, D is the drag force, L is the lift force, while the meaning of b and c is reported in Figure 4.
The effect of the abrupt change in matter's properties described above is the presence of an additional drag component, also known as wave drag,that obstructs further the forward movement of the airfoil.

In our simulation we are interested in the *steady-state* solution which we can seek as the limit of the non stationary solution for $t \to \infty$; the process is stopped when a suitable steady-state criterion is achieved.
The usual one used for explicit time discretization reads as:

$$\frac{1}{\Delta t^n} \left\| \boldsymbol{U_h^{n+1}} - \boldsymbol{U_h^n} \right\|_{L^2(\Omega)} \leq TOL$$

where TOL is a given tolerance.

Anyway since we are interested in the computation of aerodynamics coefficients of the considered flow we can employ a stopping criterion which follows from the physical nature of the considered problem.
First of all let us redefine drag and lift coefficients in integral form: they are respectively the first and the second component of the vector

$$\frac{1}{\frac{1}{2}p_\infty U_\infty^2 c} \int_{\Gamma_{prof}} p\boldsymbol{n}\, d\Sigma$$

where Γ_{prof} is the profile, $\boldsymbol{n}$ is the outer unit normal to the profile, p is the pressure and the meaning of the other symbols is explained in Figure 4.

Then it is natural to stop when these coefficients achieve a given tolerance, namely:

$$\Delta C_D \leq TOL$$
$$\Delta C_L \leq TOL$$

where

$$\Delta C_\alpha(k) = \max_{l=\bar{k},\ldots k} C_\alpha(l) - \min_{l=\bar{k},\ldots k} C_\alpha(l). \tag{5.2}$$

Here $\alpha = D, L$ for drag and lift and $C_\alpha(k)$ is the value of the corresponding aerodynamic coefficient at the kth time level and $\bar{k}$ is the entire part of the number $0.95k$. This means that the minimum and maximum in (5.1) are taken over the last 5% of the number of time levels. In contrast to the tolerance of the first criterion which has to be chosen empirically, the tolerance in this criterion can be chosen only on the basis of our accuracy requirements: if the chosen tolerance is equal to 10^{-4}, the stopping criterion gives accuracy of the aerodynamic coefficients for 3 decimal digits.

We report now the computational mesh employed in our simulations.

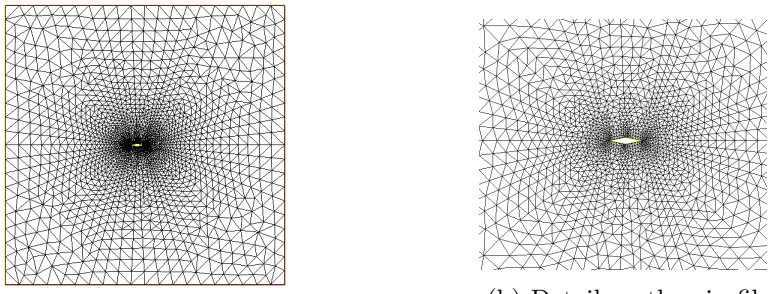

(a) Whole mesh

(b) Detail on the airofil

Figure 8: Computational mesh

The diamond profile is embedded in a rectangle which represents ideally the infinite.

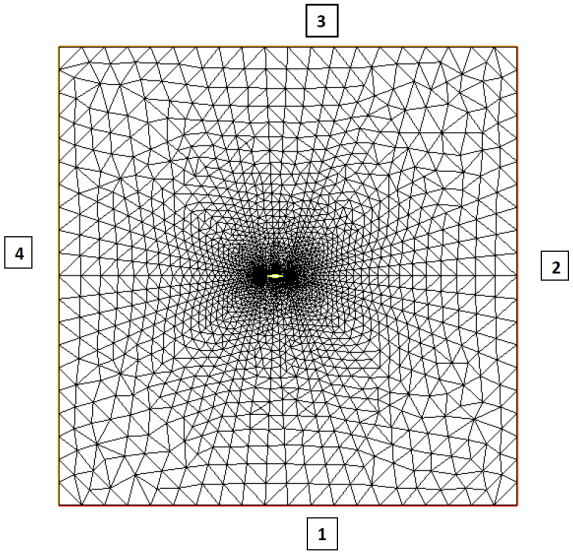

Figure 9: Boundary labels

At boundary 4 we impose supersonic inflow condition,while for the other

boundaries, considering in general positive angles of attack in the anti-clockwise direction, since our rectangle represents the infinite we can suppose that our flow is undisturbed and so we impose supersonic outflow condition at 2 and 3 and supersonic inflow condition at 1. Eventually we impose 'no-penetration condition' which means $\boldsymbol{u} \cdot \boldsymbol{n} = 0$ for the double-wedge airfoil in order to enforce impermeability.
Only in the case $\alpha = 0°$ we impose this condition also for boundaries 1 and 3.

The first attempt is made at $Ma = 1.2$ with angle of attack $\alpha = 0°$. The result is reported in Figure 10

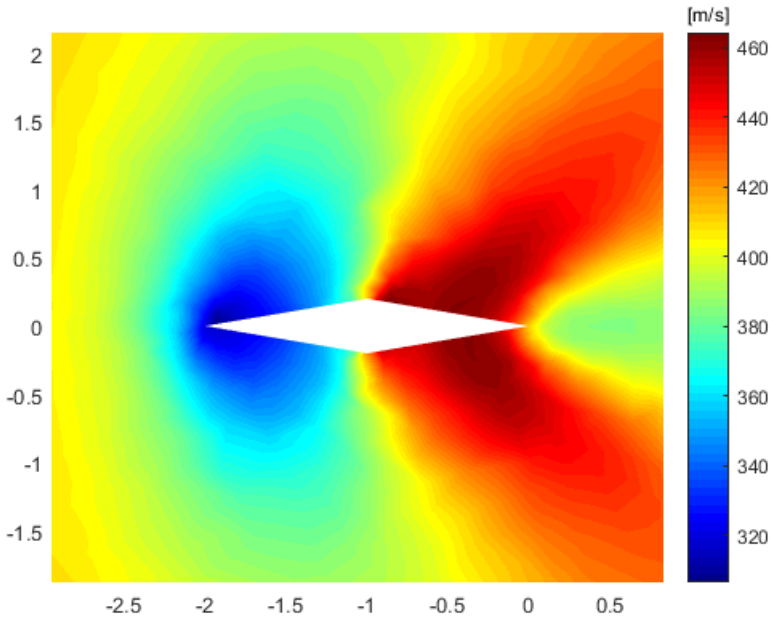

Figure 10: Velocity contour at Ma = 1.2, $\alpha = 0°$

As we can see we are in the presence of a detached flow; this result is expected from the theoretical analysis: indeed if we denote by θ the half-edge angle of our profile we have a shock wave if

$$\theta < \frac{4}{3\sqrt{3}(\gamma+1)} \frac{(Ma^2-1)^{3/2}}{Ma^2}$$

as reported in [11] and in this case

$$\arctan\left(\frac{0.2}{1.0}\right) = 0.1974 > \frac{4}{3\sqrt{3}(\gamma+1)} \frac{(1.2^2-1)^{3/2}}{1.2^2} = 0.0650$$

Therefore we need to increase the Mach number if we want to obtain a shock wave; if we set $Ma = 1.8$ we get

$$\arctan\left(\frac{0.2}{1.0}\right) = 0.1974 < \frac{4}{3\sqrt{3}(\gamma+1)}\frac{(1.8^2-1)^{3/2}}{1.8^2} = 0.3319$$

and so we expect an attached flow.

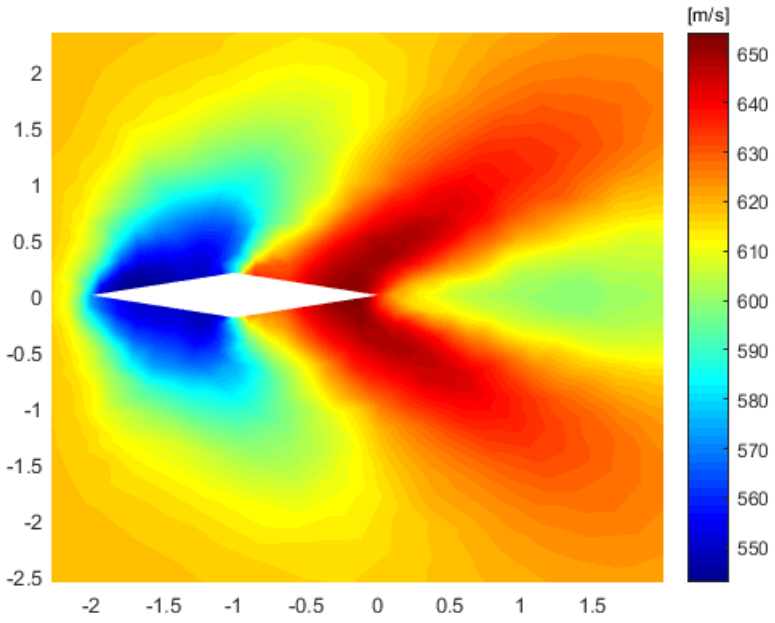

Figure 11: Velocity contour at Ma = 1.8, $\alpha = 0°$

As we can see in Figure 11 the expectations are verified. We are in the presence of two oblique shock waves and an expansion wave.

Analogous results are obtained using an angle of attack different from 0°

as reported in Figure 12 even if, obviously, in this case we have an asymmetric behaviour.

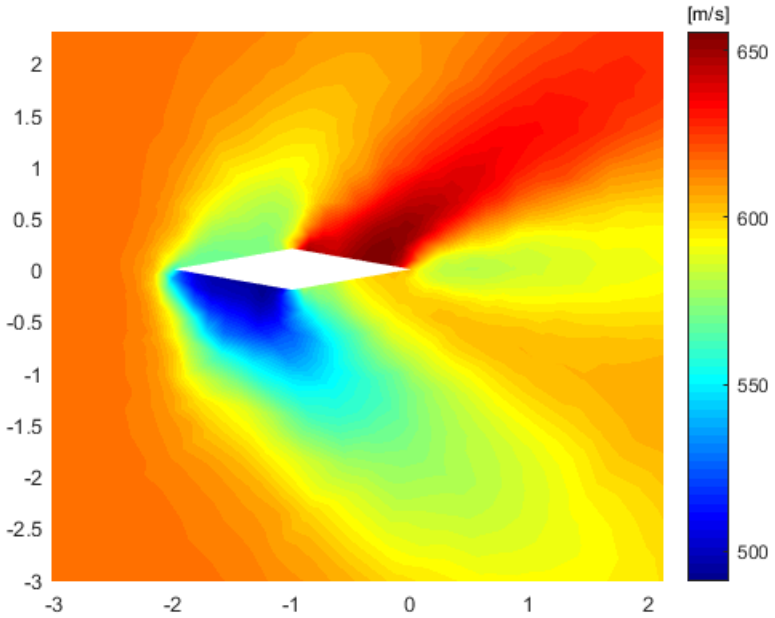

Figure 12: Velocity contour at Ma $= 1.8$, $\alpha = 5°$

Eventually we verify the behaviour of the aerodynamic coefficients; first of all we report the results obtained at $\alpha = 5°$ with different Mach numbers comparing the numerical values obtained in our simulations with theoretical values obtained from the shock theory explained before and computed with the aid of a MATLAB script.

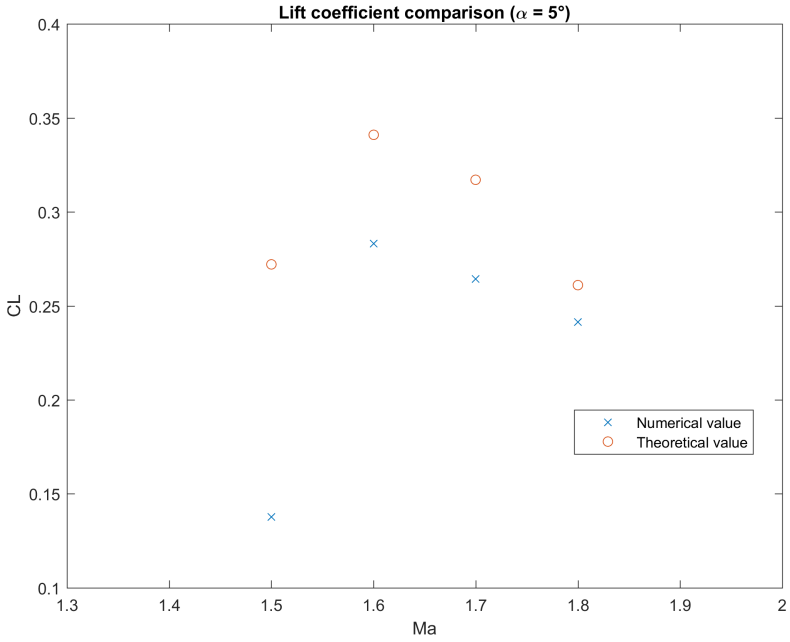

Figure 13: Lift coefficient comparison at different Mach

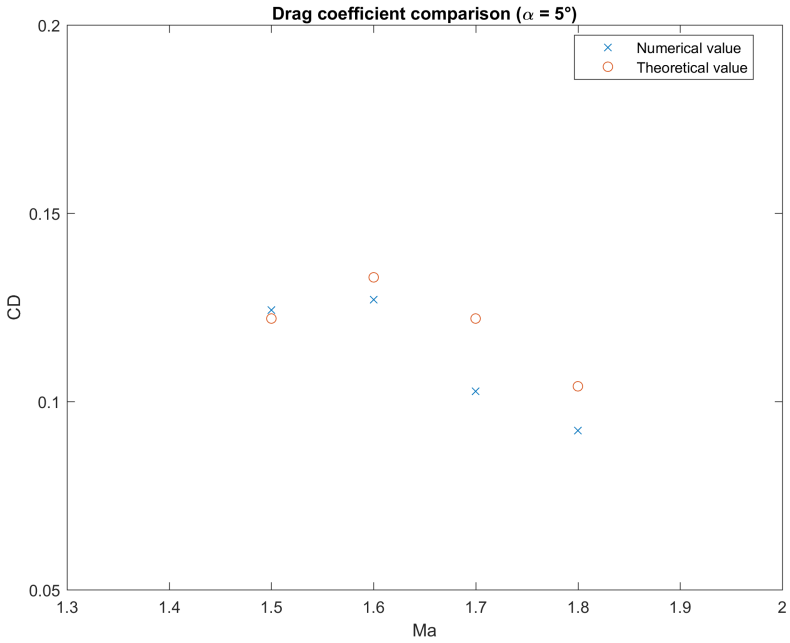

Figure 14: Drag coefficient comparison at different Mach

We see that drag coefficient is somehow predicted better than lift coefficient but in both cases the global behaviour of the coefficients is caught by the scheme especially at higher Mach numbers.

Analogous results are obtained if we fix the Mach number at 1.8 and we change the angle of attack

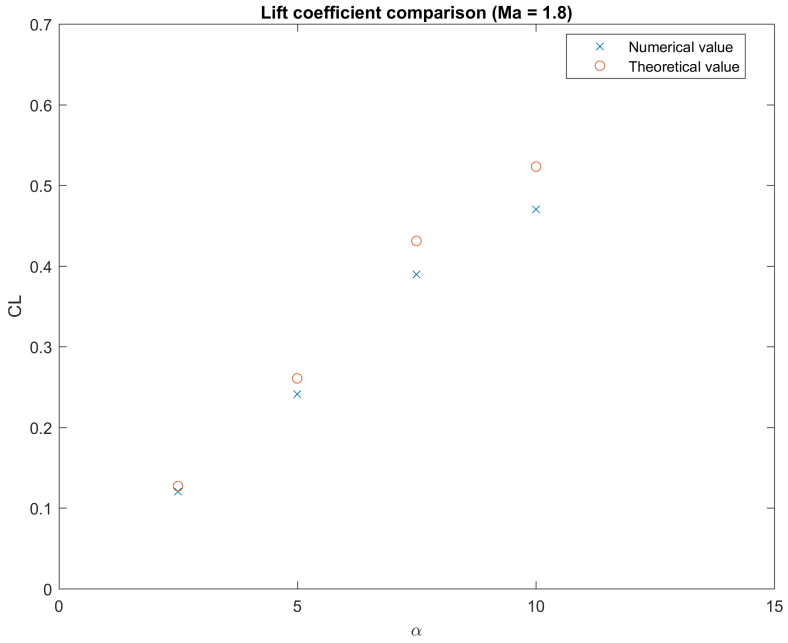

Figure 15: Lift coefficient comparison at different angles of attack

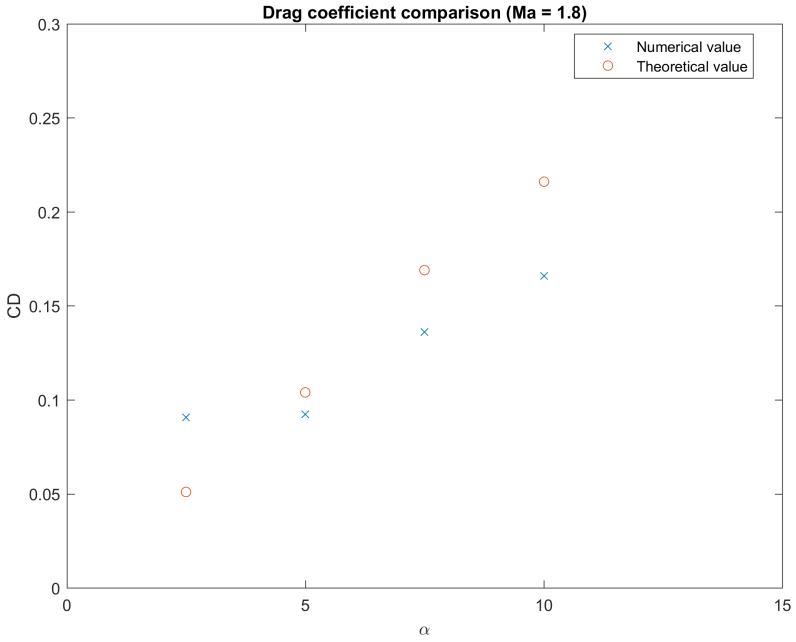

Figure 16: Drag coefficient comparison at different angles of attack

Summing up we see that lift and drag coefficients decrease with increase in Mach and decrease in angle of attack and the scheme is able to reproduce this behaviour as desired.

References

[1] B. Cockburn, C.W. Sun: Runge-Kutta Discontinuous Galerkin Methods for Convection-Dominated Problems, Journal of Scientific Computing, Volume 16, No. 3, September 2001

[2] F. Bassi, S. Rebay: High-Order Accurate Discontinuous Finite Element Solution of the 2D Euler Equations, Journal of Computational Physics,Volume 138, Issue 2, 1997, Pages 251-285,

[3] B. Cockburn: High-Order Methods for Computational Physics, Springer Berlin Heidelberg, Berlin, Heidelberg, 1999, Pages 69-224.

[4] V. Dolejsi, M.Feistauer: Discontinuous Galerkin method: analysis and applications to compressible flow, Springer, London, 2015, Chapter 8

[5] V. Dolejsi, M.Feistauer, C. Schwab: On some aspects of the discontinuous Galerkin finite element method for conservation laws. Math. Comput. Simul. 61, 333-346, 2003

[6] J. S. Hesthaven, T. Warburton, Nodal Discontinuous Galerkin Methods. Algorithms, Analysis, and Applications, Springer-Verlag, New York, 2008

[7] L. Kourous, Adaptive hp Discontinuous Galerkin Method for Nonstationary Compressible Euler Equations, Master Thesis, 2011

[8] R. Hartmann, Numerical Analysis of Higher Order Discontinuous Galerkin Finite Element Methods, Institute of Aerodynamics and Flow Technology DLR (German Aerospace Center)

[9] J. Jafree,C. Johnson,A. Szepessy, Convergence of the Discontinuous Galerkin finite element method for hyperbolic conservation laws, Math. Models Methods Appl. Sci 5(3), 367-286, 1995

[10] Oblique Shock Wave, `http://www.iaa.ncku.edu.tw/~aeromems/Mach/Ch3.pdf`

[11] Detached Normal Shock, `https://www.grc.nasa.gov/www/k-12/airplane/detach.html`